CrossMark

ORIGINAL PAPER

Acoustic and Petrophysical Evolution of Organic-Rich Chalk Following Maturation Induced by Unconfined Pyrolysis

Omri Shitrit[1] · Yossef H. Hatzor[1] · Shimon Feinstein[1] · Harold J. Vinegar[1,2]

© Springer-Verlag GmbH Austria 2017

Abstract Thermal maturation is known to influence the rock physics of organic-rich rocks. While most studies were performed on low-porosity organic-rich shales, here we examine the effect of thermal maturation on a high-porosity organic-rich chalk. We compare the physical properties of native state immature rock with the properties at two pyrolysis-simulated maturity levels: early-mature and over-mature. We further evaluate the applicability of results from unconfined pyrolysis experiments to naturally matured rock properties. Special attention is dedicated to the elastic properties of the organic phase and the influence of bitumen and kerogen contents. Rock physics is studied based on confined petrophysical measurements of porosity, density and permeability, and measurements of bedding-normal acoustic velocities at estimated field stresses. Geochemical parameters like total organic carbon (TOC), bitumen content and thermal maturation indicators are used to monitor variations in density and volume fraction of each phase. We find that porosity increases significantly upon pyrolysis and that P wave velocity decreases in accordance. Solids density versus TOC relationships indicate that the kerogen increases its density from 1.43 to 1.49 g/cc at the immature and early-mature stages to ~ 2.98 g/cc at the over-mature stage. This density value is unusually high, although increase in S wave velocity and backscatter SEM images of the over-mature samples verify that the over-mature kerogen is significantly denser and stiffer. Using the petrophysical and acoustic properties, the elastic moduli of the rock are estimated by two Hashin–Shtrikman (HS)-based models: "HS + BAM" and "HS kerogen." The "HS + BAM" model is calibrated to the post-pyrolysis measurements to describe the mechanical effect of the unconfined pyrolysis on the rock. The absence of compaction in the pyrolysis process causes the post-pyrolysis samples to be extremely porous. The "HS kerogen" model, which simulates a kerogen-supported matrix, depicts a compacted version of the matrix and is believed to be more representative of a naturally matured rock. Rock physics analysis using the "HS kerogen" model indicates strong mechanical dominance of porosity and organic content, and only small maturity-associated effects.

Keywords Porosity · Kerogen · Bitumen · Rock physics · Pyrolysis · Thermal maturation

1 Introduction

Oil and gas are known to originate from organic-rich sedimentary rocks and therefore are defined as source rocks. The organic phases in source rocks typically include kerogen (solid) and bitumen (quasi-liquid), where their properties and proportions vary upon thermal maturation. The organic material is distributed in a fine-grained matrix of various lithologies, like clay-rich shales (e.g., Bakken, Kimmeridge), marls (Eagle Ford), porcelanites (Monterey) and chalks (Niobrara, Ghareb–Mishash) (Avseth and Carcione 2015; Baskin and Peters 1992; Bisnovat et al. 2015; Bridges 2016; Sone and Zoback 2013). During maturation, the organic material is exposed to elevated temperature and pressure and decomposes to release volatile hydrocarbons, which may migrate and accumulate in a conventional

✉ Omri Shitrit
  shitrit@post.bgu.ac.il

1 Department of Geological and Environmental Sciences, Ben-Gurion University of the Negev, 84105 Beer-Sheva, Israel

2 Israel Energy Initiatives Ltd, 5 Shlomo HaLevi Street, 91450 Jerusalem, Israel

reservoir rock. If migration is prevented, the source rock becomes a self-sourcing reservoir. Immature source rocks are also potential reservoirs as in situ heating methods are used to introduce thermal maturation. For these reasons, rock physics studies of source rocks are of great interest for exploring conventional and unconventional oil and gas plays. Evaluation of organic-rich rocks from surface seismics and well logs is based on the dependence of rock properties on organic content and maturation (Bredesen et al. 2015; Løseth et al. 2011). In this paper, we aim to establish maturity-dependent modeling of organic-rich chalks, based on laboratory experiments.

The interaction of thermal maturation with field conditions (e.g., stress field, pore pressure, host rock properties, temperature) makes source rock dynamics exceptionally complex. Numerous rock physics studies have been carried out on source rocks, specifically on organic-rich shales (e.g., Avseth and Carcione 2015; Carcione, Helle and Avseth 2011; Sayers 2013; Sone and Zoback 2013; Suarez-Rivera and Fjær 2013; Vanorio, Mukerji and Mavko 2008; Vernik and Nur 1992; Zhao et al. 2016). The elastic properties of organic-rich shales were studied with great attention to organic content, clay content, microcracks, and porosity. Specific treatment has been dedicated to clay mechanics, such as mineral transformations, clay-bound water and rock fabric (Carcione and Avseth 2015; Qin et al. 2016; Villamor et al. 2016). A typical shale model assumes layered microstructure with low porosity, so that Backus-type averaging is commonly used (Carcione et al. 2011; Vernik and Nur 1992; Zhao et al. 2016). However, the applicability of these models to organic-rich chalks with high porosity seems questionable. It is known that rock physics modeling should incorporate geological information to account for differences in facies and rock texture (Avseth et al. 2010). The porosity of organic-rich chalks includes stiff intra-calcite porosity and inter-granular porosity with small grain-contact area. Porosity in clay-rich shales on the other hand comprises compliant inter-particle and intra-clay porosity in a sheeted fabric (Loucks et al. 2012); hence, shales tend to be much less porous than chalks. Therefore, unlike most source rocks, rock physics modeling of organic-rich chalks needs to be chalk-oriented. Chalks are frequently modeled using Hashin–Shtrikman-based methods like isoframe (Fabricius 2003; Fabricius et al. 2010) and Marion's bounding average method (BAM, Marion 1990; Shitrit et al. 2016, 2017). A detailed overview of chalk models is given in Olsen (2007). In this paper, we apply Hashin–Shtrikman-based models to identify microstructural features of the organic-rich chalk at three different maturity levels.

The evolution of entire rock properties during maturation is closely related to changes occurring in the organic matter if the organic content is sufficiently high (Labani and Rezaee 2015). Specifically, in sulfur-rich kerogens (typically type

IIS) the kerogen first produces bitumen, and upon maturation the oil and gas originate mostly from decomposition of the generated bitumen (Baskin and Peters 1992). It is known that upon maturation, the density and stiffness of the kerogen are increased (Alfred and Vernik 2012; Emmanuel et al. 2016; Zargari et al. 2013). On the other hand, the newly generated kerogen porosity is filled with bitumen, oil and gas, which may cause an overall softening of the organic phase (Eliyahu et al. 2015; Modica and Lapierre 2012; Zargari et al. 2016). Solid residues like graphite, pyrite and pyrobitumen may form during maturation as well (Bernard et al. 2012; Modica and Lapierre 2012; Zhao et al. 2016). Therefore, rock physics studies of differentially matured rocks account for these maturity-associated variations. Commonly, organic-rich rocks are found at a specific level of maturation, so in order to examine rock properties at various maturity levels pyrolysis is used to induce maturation (Allan et al. 2014; Bisnovat 2013; Gayer 2015; Zargari et al. 2013).

In this study, we use core samples to investigate the effect of maturity on the organic-rich chalk of Late Cretaceous Ghareb and Mishash formations. Maturation is induced by unconfined, anhydrous pyrolysis. The core samples are taken from the Zoharim well in the Shefela basin in Israel, on which sedimentological, geochemical, petrophysical and mechanical studies have been recently performed (Bisnovat et al. 2015; Gordin et al. 2016; Kutuzov 2017; Meilijson et al. 2014; Shitrit et al. 2016, 2017). The rock is buried to shallow depths of several hundreds of meters and considered to be immature. The organic phase mainly includes a kerogen classified as type IIS, due to high total sulfur (TS) content. The immature organic-rich chalk exhibits high porosity (20–45%) and high total organic carbon content (TOC, up to 20 %wt), both of which strongly influence the static and dynamic elastic properties. In this paper, we use measurements of native state and pyrolyzed core samples to examine the effect of maturity on rock properties (namely petrophysical and elastic properties). The goal is to study the maturation process in the organic-rich chalk and improve predictive abilities of organic content and maturity from surface seismics and well logs.

2 Methods

2.1 Petrophysical Properties and Elastic Moduli

Measurements of petrophysical and acoustic properties were taken on core samples at immature (native) state, early-mature state and over-mature state (post-pyrolysis). These measurements were taken on 1-inch-length and 1-inch-diameter core plugs. Following sample preparation, each plug was first dried in an oven (24 h in 105 °C) and then measured for the petrophysical properties.

Subsequently, the plugs were saturated with brine and measured for the acoustic velocities. Post-pyrolysis samples were taken from the pyrolysis reactor directly to desiccator to maintain the dry conditions and then went through the same sequence of petrophysical and acoustic measurements. To analyze the influence of organic content, TOC measurements were taken by IEI (using a SC632 LECO device) on pieces from each core sample at each maturity level. Description of the petrophysical and acoustic measurements is presented in this section. General description of the experimental conditions is given in Table 1.

Petrophysical measurements included porosity, Klinkenberg-corrected gas permeability and solids density, measured in a Coreval30 poropermeameter manufactured by Vinci Technologies. The dry core plugs were surrounded by an elastomer sleeve, and a confining pressure of 400 psi (2.8 MPa) was applied. Porosity and solids density measurements followed the "Boyle's law single-cell method" in API recommended practice for core analysis (Sect. 5.3.2.2.1 in American Petroleum Institute (API) 1998). Permeability measurements were taken using the "pressure-falloff, axial gas flow" technique, according to API recommended practice (Sect. 6.4.1.1 in American Petroleum Institute (API) 1998). This method is based on Klinkenberg's gas slippage theory (Klinkenberg 1941), allowing conversion from gas permeability to an apparent liquid permeability:

$$K_1 = \frac{K_g}{1 + \frac{4c\bar{\lambda}}{\bar{r}}} \tag{1}$$

where K_1 and K_g are the permeability of the rock to liquid and gas, respectively, c is a dimensionless gas slippage coefficient (approximately 1), $\bar{\lambda}$ is the mean free path of the gas molecules (~ 61 nm for nitrogen at room conditions), and $\bar{r}$ is the average pore radius.

In horizontally bedded sediments, it is acceptable to consider the elasticity of the rock to exhibit vertical transverse isotropy (VTI). Therefore, acoustic velocities are typically calculated using the five characteristic stiffness constants (Mavko et al. 2009):

$$C_{11} = \rho_b V_{p90}^2; \; C_{33} = \rho_b V_{p0}^2; \; C_{55} = \rho_b V_{s0}^2; \; C_{66} = \rho_b V_{sH90}^2$$

$$C_{13} = \sqrt{\left(2\rho_b V_{p45}^2 - C_{11} - C_{55}\right)\left(2\rho_b V_{p45}^2 - C_{33} - C_{55}\right)} - C_{55} \tag{2}$$

where ρ_b is bulk density, V_{p0}, V_{p45} and V_{p90} are the P wave velocities in the bedding-normal, bedding-diagonal and bedding-parallel directions, respectively, and V_{s0} and V_{sH90} are the S wave velocities in the bedding-normal and the fast bedding-parallel directions, respectively. In this paper, we focus on the bedding-normal P wave modulus C_{33} (also referred as vertical oedometer modulus "M_v"), and the vertical S wave modulus C_{55} (also referred as vertical shear modulus, "μ_v"). The acoustic velocities were measured in the Acoustic Velocity System (AVS350) manufactured by Vinci Technologies. The AVS350 system is designed for ultrasonic wave velocities, with piezoelectric transducers vibrating at a center frequency of 500 kHz. Individual control on axial, radial, and pore pressures allowed us to replicate field conditions. Brine-saturated plugs were measured under axial, radial and pore pressures that were assumed to be the vertical stress, minimum horizontal stress and pore pressure in the field, respectively, as estimated from hydraulic jacking tests (Golder Associates 2011). The vertical stress was estimated to increase linearly with depth from 6.1 MPa at formation top to 12.1 MPa at formation bottom, and the pore pressure increased hydrostatically from 2.9 to 5.6 MPa. The minimum horizontal stress was tested in four different

Table 1 General description of testing conditions in both native state and post-pyrolysis samples

Type of measurements	Measured properties	Sample	Pressure conditions	Saturated/dry
Petrophysics	Porosity Solids density Permeability	Core plug 1″ long 1″ diameter	*Confining pressure* 400 psi (2.8 MPa)	Dry
Acoustics	*P* wave velocity (V_p) *S* wave velocity (V_s)	Core plug 1″ long 1″ diameter	*Axial pressure* in situ vertical stress[b] *Radial pressure* in situ min. horizontal stress[b] *Pore pressure* in situ pore pressure[b]	Saturated with brine
Geochemistry[a]	TOC, TS, B_c, %Ro, T_{max}, HI	Crushed powder	None	Dry

[a]Measured data by IEI Ltd. and Kutuzov (2017)

[b]Field stress estimations according to hydraulic jacking tests by Golder Associates (2011)

depth intervals, and linear interpolations were used to estimate the minimum horizontal stress at each depth, ranging from 3.7 to 7.5 MPa. A more detailed depth profile of the stresses may be found in Shitrit et al. (2016). The brine had a salinity of 0.6 mgNaCl/g.

The brine-saturated data published in our previous study (Shitrit et al. 2016) allowed us to obtain the vertical oedometer modulus and the vertical shear modulus at the immature state. Here we combine Hashin–Shtrikman (HS) bounds with Marion's bounding average method (Marion 1990) in order to create a general model for each maturity stage, calibrated to the measured moduli. The HS upper and lower bounds of bulk and shear moduli, which represent the stiffest and softest possible arrangement of the phases in the rock, respectively, are given by Mavko et al. (2009):

$$K_{HS}^{+/-} = \left(\sum_{i=1}^{n} \frac{f_i}{K_i + \left(\frac{4}{3} \mu_{max/min} \right)} \right)^{-1} - \frac{4}{3} \mu_{max/min} \qquad (3)$$

$$\mu_{HS}^{+/-} = \left(\sum_{i=1}^{n} \frac{f_i}{\mu_i + \left(\zeta_{max/min} \right)} \right)^{-1} - \zeta_{max/min} \qquad (4)$$

where "+" and "−" are the upper and lower bounds, f_i is the volume fraction of each phase, and max and min refer to the theoretical moduli of the stiffest and softest phases, respectively. The ζ of each phase is calculated by Mavko et al. (2009):

$$\zeta = \frac{\mu}{6} \left(\frac{9K + 8\mu}{K + 2\mu} \right) \qquad (5)$$

We used the minerals elastic moduli as max, calculated by the average minerals distribution and the individual modulus of each mineral (Table 2). For the lower bound (simulating a fluid-suspended matrix), we used the elastic moduli of the brine as min. An additional Hashin–Shtrikman intermediate curve ("HS kerogen") was calculated as well to simulate a kerogen-supported matrix (defined in Shitrit et al. 2017). This was done by introducing the shear modulus of kerogen in Eq. (3) and the μ and ζ of kerogen in Eq. (4). Theoretical elastic moduli of the kerogen at the three maturity levels are summarized in Table 2 and further explained in the results section. Using Eqs. (3) and (4), the bounds of the oedometer modulus were calculated:

$$M = K + \frac{4}{3} \mu \qquad (6)$$

The relative position of the measured moduli between the upper and lower bounds is described by the normalized

Table 2 Elastic moduli of rock components

Mineral	%v	K (GPa)	μ (GPa)
Kaolinite	1	44.2	22.1
Illite	1	60.2	25.4
Smectite	8	9.3	6.9
Calcite	61	71	30
Dolomite	1	80	48
Quartz	4	37	45
K-spar	1	37.5	15
Plag	1	75.6	25.6
Pyrite	1	147	132
Apatite	20	85	46
Minerals average		66	32
Kerogen: immature		5.7	2.6
Kerogen: early-mature		6	2.7
Kerogen: over-mature		10.3	4.4
Bitumen		3.5	0.7
Brine		2.32	0

Minerals moduli are taken from Mavko et al. (2009), clay minerals specifically from Wang et al. (2001) and volume percentage of each mineral in the organic-rich chalk from X-ray diffraction analysis (Average distribution was provided by IEI Ltd.). Elastic properties of kerogen at different maturity levels are modified based on the values reported in Eliyahu et al. (2015) and Emmanuel et al. (2016), assuming a Poisson's ratio of 0.3. The elastic properties of bitumen are taken from Han et al. (2006)

stiffness factor (w), as defined in Marion's BAM fluid substitution model (Marion 1990):

$$w = \frac{A - A^-}{A^+ - A^-} \qquad (7)$$

where A represents each modulus being computed (e.g., M, K, μ). The "w" of each modulus is a characteristic of the geometrical arrangement of the phases and may be used for modeling when calibrated with experimental data. This combined model is referred here as "HS + BAM."

2.2 Unconfined, Anhydrous Pyrolysis Experiments

Pyrolysis experiments were performed in order to induce thermal maturation in the organic-rich chalk samples. Unconfined pyrolysis experiments were performed in semi-open dry pyrolysis reactors (Model 4622 Parr Instruments Inc., USA). The pyrolysis experiments were performed with backpressure maintained at atmospheric level throughout the entire process; therefore, the pyrolysis is referred to as "unconfined." The maturation was induced in the absence of water (as in Ryan et al. 2010); hence, the pyrolysis is defined as "anhydrous." The pyrolysis experiments (performed by IEI Ltd.) were conducted in the organic geochemistry laboratory at Ben-Gurion University of the Negev (BGU).

The immature core samples were placed in the pyrolysis reactors, and crushed powder of the rock was spread in the voids between the plugs to reduce free spaces and optimize temperature equilibration in the pyrolysis cell. After sealing the cells, the rocks were flushed several times with nitrogen gas to expel all oxygen from rock pores and dead spaces in the system. The pyrolysis reactors were equipped with three heating elements to maintain homogeneous temperature inside the cell. Heating was conducted at two stages. First, temperature was elevated rapidly (25 °C/day) up to ~ 200 °C and kept for several hours to ensure soaking of the interstitial and rock pore water. Subsequently, the temperature was elevated at a slow rate (2 °C/day), until the target temperatures were achieved. The results of two pyrolysis experiments are presented in this paper: experiment Ex41 which terminated at 276 °C to simulate early maturation; and experiment Ex42 which terminated at 377 °C to simulate over-maturation. In Ex42, heating was stopped when volatile hydrocarbon detection at the outlet declined to zero. At that stage, the temperature was cooled down to room temperature, and the post-pyrolysis samples were collected.

Table 3 presents geochemical data for thermal maturity level of the three sets of samples studied. The most commonly reported maturity parameters are vitrinite reflectance (%Ro), and Rock–Eval pyrolysis parameters T_{max} and hydrogen index (HI). Note that the use of HI alone as a maturity parameter can be misleading, because its value depends on the initial hydrocarbon total potential and on the type of the organic matter (Vanorio et al. 2008). Thermal maturation of the studied rock samples at their native state is immature, characterized by very low T_{max} (412 °C) determined from Rock–Eval analysis, which corresponds to vitrinite reflectance of %Ro = 0.32 (Kutuzov 2017). The maturation levels attained through the pyrolysis experiments were estimated by Rock–Eval T_{max} measurements, and equivalent %Ro was calculated by Kutuzov (2017) from the pyrolysis heating history using the "Easy %Ro" model (Sweeney and Burnham 1990). Both the T_{max} measurements and the %Ro estimations indicate an early-mature state for the samples in Ex41 and over-mature state for the samples from Ex42 (Table 3). The early and high maturity levels are further corroborated by the changes in TOC and

HI compared to the immature state: relatively low reduction in TOC and HI in Ex41, and very prominent depletion of the TOC and HI in Ex42.

2.3 Densities and Volume Fractions

The organic-rich chalk is a high-porosity mixture of organic and inorganic components. The organic phase at the immature state is primarily composed of kerogen, with negligible amounts of bitumen. Upon maturation of type IIs kerogen, the kerogen decomposes to bitumen and bitumen decomposes to volatile hydrocarbons. In past rock physics studies on organic-rich rocks, TOC was often converted straightforwardly to kerogen content (e.g., Carcione and Avseth 2015; Sone and Zoback 2013; Vernik and Nur 1992). However, the presence of bitumen within the organic phase should not be ignored as it may alter rock properties such as elastic moduli, porosity, permeability and solids density. It is verified that bitumen has different elastic moduli than kerogen (Eliyahu et al. 2015); thus, distinction between kerogen and bitumen is preferable. In this section, we show a scheme for calculating densities and volume fractions of the phases by using porosity, density and TOC data. Further derivation of bitumen and kerogen concentrations is enabled by results of bitumen extraction experiments (Kutuzov 2017). It should be noted that bitumen in the samples is read as part of the solid phase in the Coreval30 porosity measurements, even though it is practically a pore-filling liquid.

In the derivation shown below, bulk volume fractions are designated by f, masses by m, and densities by ρ, and the subscripts "s", "m", "o", "k" and "bit", respectively, refer to the solids, minerals, organic matter, kerogen and bitumen. By combining the dry rock density with the measured porosity, solids density is obtained ($\rho_s = \frac{\rho_{dry}}{1-\varphi}$). We previously showed (Shitrit et al. 2016) that the solids density versus TOC relationship can be described by the following trend:

$$\rho_s = \frac{a_1}{1 + a_2 \text{TOC}} \tag{8}$$

Table 3 Organic content and maturity parameters of the three investigated maturity groups

	Average TS (%wt)	TOC loss rate (%)[a]	B_c[b]	%Ro	T_{max} (°C)	HI $\left(\frac{\text{mgHC}}{\text{gTOC}}\right)$	Maximum pyrolysis temperature (°C)
Immature (native state)	2.12	–	0.06	0.32	412	652	–
Early-mature (Ex41)	1.56	3.3	0.3	0.64[c]	421	650.5	276
Over-mature (Ex42)	0.89	32	0.3	1.57[c]	496	55	377

[a]Loss is calculated by: $\frac{\text{TOC}_{post\text{-}pyrolysis} - \text{TOC}_{pre\text{-}pyrolysis}}{\text{TOC}_{pre\text{-}pyrolysis}}$

[b]B_c, bitumen volumetric fraction of the organic matter

[c]Vitrinite reflectance equivalent values, determined using "Easy %Ro" (Kutuzov 2017)

where $a_1 = \rho_m$, $a_2 = \frac{\frac{\rho_m}{\rho_o} - 1}{C_{pr}}$, and C_{pr} is the carbon weight percentage in the organic matter. By fitting Eq. (8) to the experimental data at each maturity stage, we can derive the average minerals density ρ_m, and the organic matter density ρ_o (by assuming a value of C_{pr}). Then, the volume fractions of minerals (f_m) and organic matter (f_o) can be estimated:

$$f_m = \frac{\rho_s}{\rho_m}(1 - \varphi)\left(1 - \frac{\text{TOC}}{C_{pr}}\right) \tag{9}$$

$$f_o = 1 - \varphi - f_m \tag{10}$$

where φ is the porosity. Estimation of bitumen and kerogen concentration is enabled using bitumen extraction data. We use here the bitumen extraction results by Kutuzov (2017), which were measured on the same native state and post-pyrolysis material, using a Soxhlet extractor and a dichloromethane/methanol (9:1 v/v) mixture for 72 h. The results were reported as the ratio between mass loss following bitumen extraction over the initial mass, referred here as BIT:

$$\text{BIT} = \frac{m_{bit}}{m_s} \tag{11}$$

Consequently, the bitumen volume fraction of the organic matter, B_c, can be written as:

$$B_c = \frac{f_{bit}}{f_o} = \frac{\text{BIT}}{\text{TOM}} \cdot \frac{\rho_o}{\rho_{bit}} \tag{12}$$

where $\text{TOM} = \frac{\text{TOC}}{C_{pr}}$, and the TOC was measured on the material before the bitumen extraction. Note that the bitumen density cannot be measured accurately because the extracted bitumen is diluted; therefore, ranges of bitumen densities are examined in this study. The phase diagram is now completed using bitumen and kerogen fractions and kerogen density:

$$f_{bit} = B_c f_o \tag{13}$$

$$f_k = f_o - f_{bit} \tag{14}$$

$$\rho_k = \frac{\rho_o f_o - \rho_{bit} B_c f_o}{f_k} \tag{15}$$

A schematic phase diagram is given in Fig. 1, showing the volume fraction and density of each component.

3 Results

3.1 Petrophysical Properties

The petrophysical properties are strongly influenced by the geochemistry of the organic matter (key features are given in
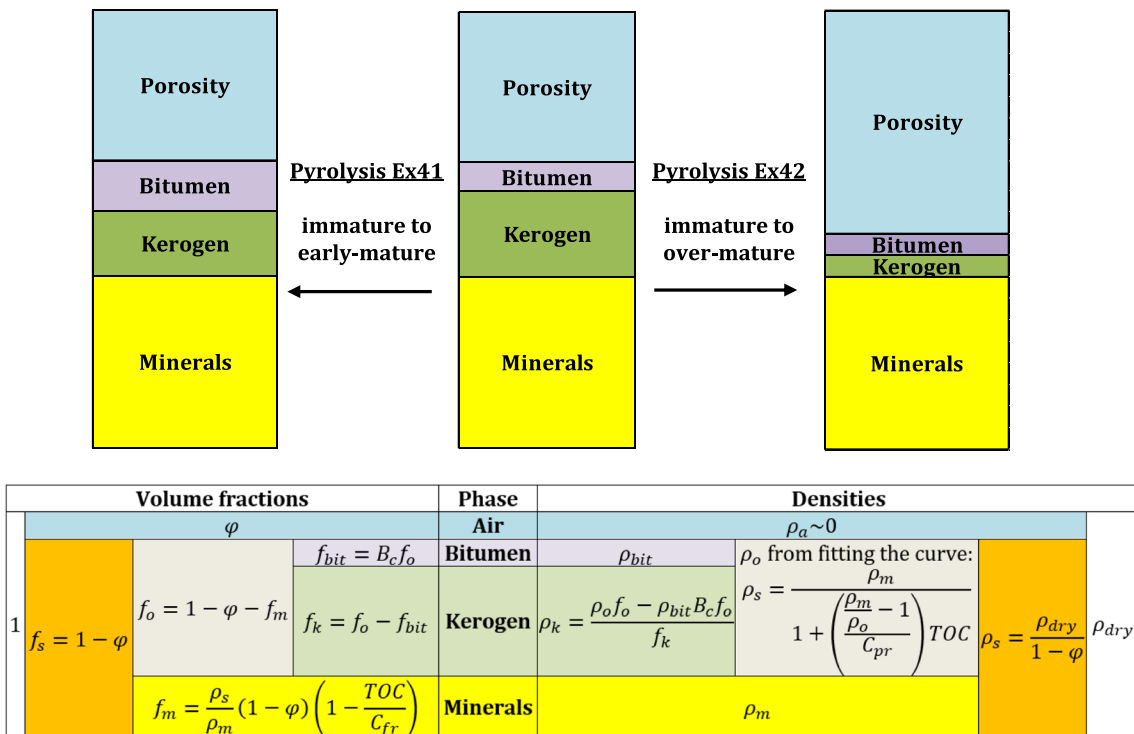

Fig. 1 Volume fractions in the studied material: schematic drawing of changes in volume of each phase at each simulated maturity stage (top). Volume fractions and densities are solved using the phase diagram suited for the organic-rich chalk (bottom). Derivation of the equations is given in Sect. 2.3

Table 3). TOC data were collected for each plug separately. The post-pyrolysis material contains significant amounts of bitumen that affect the petrophysical measurements. By considering the bitumen as a pore-filling liquid, the true porosity (φ_t) is the sum of the measured porosity and the bitumen fraction ($\varphi_t = \varphi_{meas.} + f_{bit}$). As seen in Fig. 2a, the bitumen causes negligible underestimation of the porosity at the immature and over-mature rock samples, and a significant underestimation (~ 12%) of the true porosity at the early-mature state. In this section, the presented porosity and solids density are the measured values and not the true values, and the pore space occupied by bitumen is being accounted for in the interpretation. Gas permeability is always higher than the liquid permeability (Fig. 2b), and the magnitude of that difference depends on the mean pore radius (Eq. 1), assuming that the proportionality factor "c" remains constant. The resulted mean pore radius of the immature rock is at the order of 500 nm, while that of the early-mature and over-mature samples is at the order of 200 nm. It should be noted here that permeability measurements of the post-pyrolysis samples yield the effective permeability to nitrogen and not the total permeability of the rock, as the bitumen interferes with nitrogen flow in the sample. This issue will be addressed in the discussion.

The measured solids density displays well the changes in physical properties of the organic material, by being directly related to TOC (Eq. 8). Solids density and TOC measurements are used to create the best-fit trendline and to obtain the fitting coefficients a_1 and a_2 for each maturity stage. We previously showed (Shitrit et al. 2016) that at the immature state a_1 is the minerals density and equals 2.74 g/cc, and by assuming $C_{pr} = 70$ the value of $a_2 = 0.0131$ leads to organic material density of 1.43 g/cc (Fig. 3). Bitumen volume fraction in the organic matter (B_c) is about 6%, within a bitumen density range of 1.0–1.1 g/cc (Baskin and Peters 1992; Han et al. 2006; Hofmann 2006; Orr 1986; Wang et al. 2010). Consequently, according to Eqs. (13), (14) and (15) the kerogen density is 1.46–1.47 g/cc. We apply the same methodology here to the post-pyrolysis data. The stability of calcite and the low clay content of the rock samples allow us to assume that the pyrolysis did not cause much alterations in the inorganic phase; thus, we can assume the minerals density remains nearly constant throughout the pyrolysis.

At the early-mature state $a_2 = 0.0147$ (Fig. 3), and by assuming $C_{pr} = 70\%$ (TOC loss is negligible), the organic matter density is 1.34 g/cc. Using bitumen densities of 1.0–1.1 g/cc, we find that $B_c = 29 - 32\%$, and thus, kerogen density is 1.44–1.51 g/cc. Only small changes in the measured solids density are observed (Fig. 4), and because the TOC loss in this pyrolysis experiment is very small, we infer that most of the initial mass of the organic matter remained inside the rock. Very slight decrease in the measured solids density (including the bitumen) may indicate that the
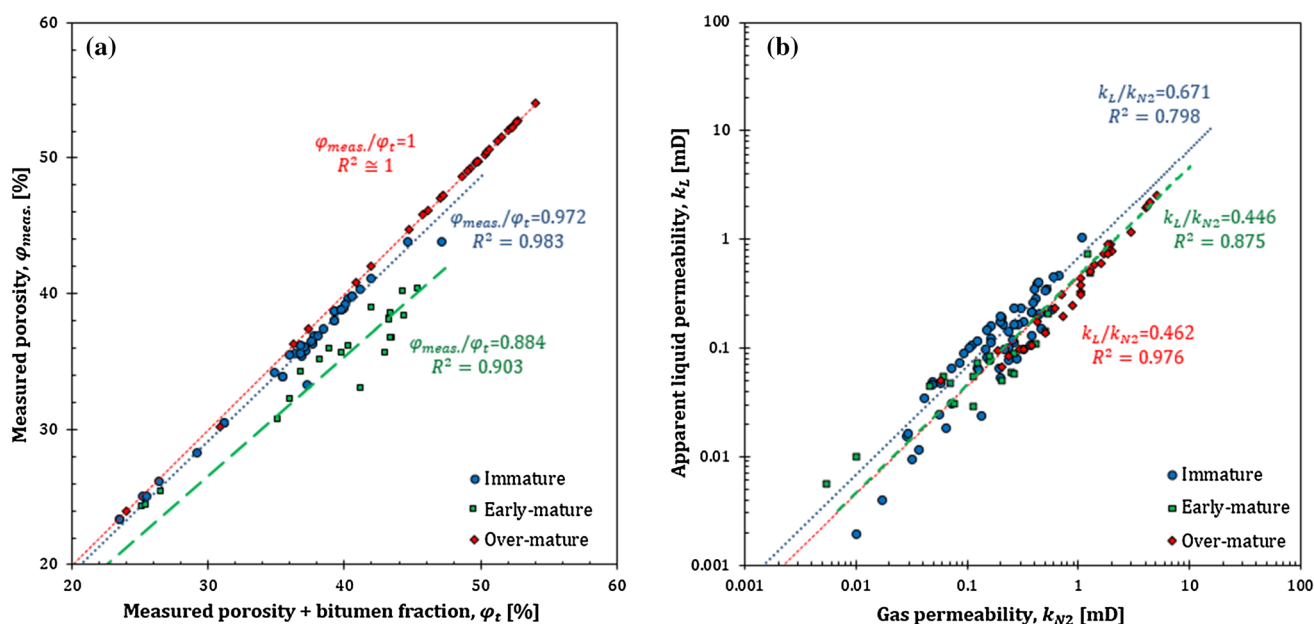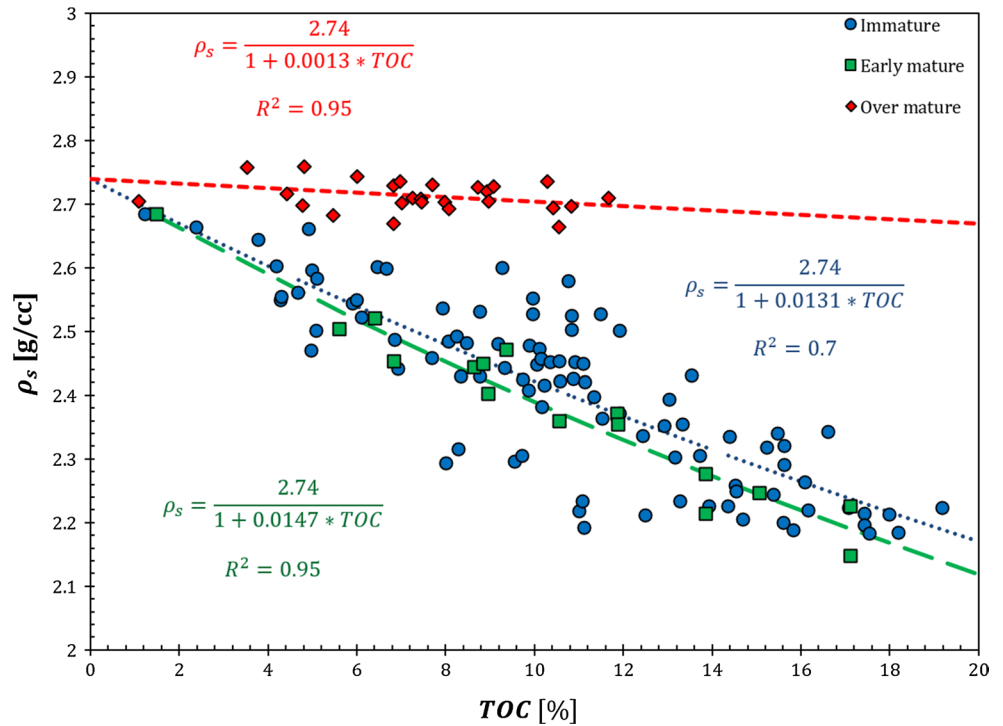

Fig. 2 Experimental deviations due to bitumen content: **a** the measured porosity ($\varphi_{meas.}$) underestimates the true porosity (φ_t) due to bitumen content, thus corrected by: $\varphi_t = \varphi_{meas.} + f_{bit}$. Bitumen volume fractions (f_{bit}) are calculated using Eqs. (12)–(13) with $B_c = 0.06$ at the immature state and $B_c = 0.3$ at the early-mature and over-mature states. **b** The ratio of apparent liquid permeability to gas permeability (K_L/K_{N2}) at the early-mature and over-mature states indicates a significant bitumen content that causes the mean radius of the bitumen-free pores to decrease from ~ 500 nm at the immature state to ~ 200 nm at the early-mature and over-mature stages

Fig. 3 Solids density versus TOC relationships at each maturity stage: trendlines are made using Eq. (8). The minerals density is set at a constant value of 2.74 g/cc. The values of the fitting coefficient a_2 depend on carbon percentage (C_{pr}) and organic matter density (ρ_o) at each maturity level

$$\rho_s = \frac{2.74}{1 + 0.0013 * TOC}$$

$$R^2 = 0.95$$

$$\rho_s = \frac{2.74}{1 + 0.0131 * TOC}$$

$$R^2 = 0.7$$

$$\rho_s = \frac{2.74}{1 + 0.0147 * TOC}$$

$$R^2 = 0.95$$

organic phase expanded, as bitumen formed at the expense of kerogen. Similar trends are seen in the measured porosity (Fig. 5), where post-pyrolysis porosity is slightly lower than the pre-pyrolysis porosity because of mild bitumen invasion into pre-existing pores. The true porosity (φ_t) is enhanced by a factor of 1.09. The apparent liquid permeability is more scattered and yet indicates no significant variations (Fig. 6a). Note that the apparent permeability tends to decrease where

initial TOC is greater than 10%, (Fig. 6b), presumably due to bitumen interference with fluid flow.

At the over-mature state $a_2 = 0.0013$ (Fig. 3), and using a typical over-mature value of $C_{pr} = 85\%$ (Vernik and Milovac 2011), the organic matter density is 2.4 g/cc. Using bitumen densities of 1.0–1.1 g/cc, we find that $B_c = 30 - 33\%$, and thus, kerogen density is 2.91–3.05 g/cc. The high density of the organic matter and the TOC loss cause the solids density
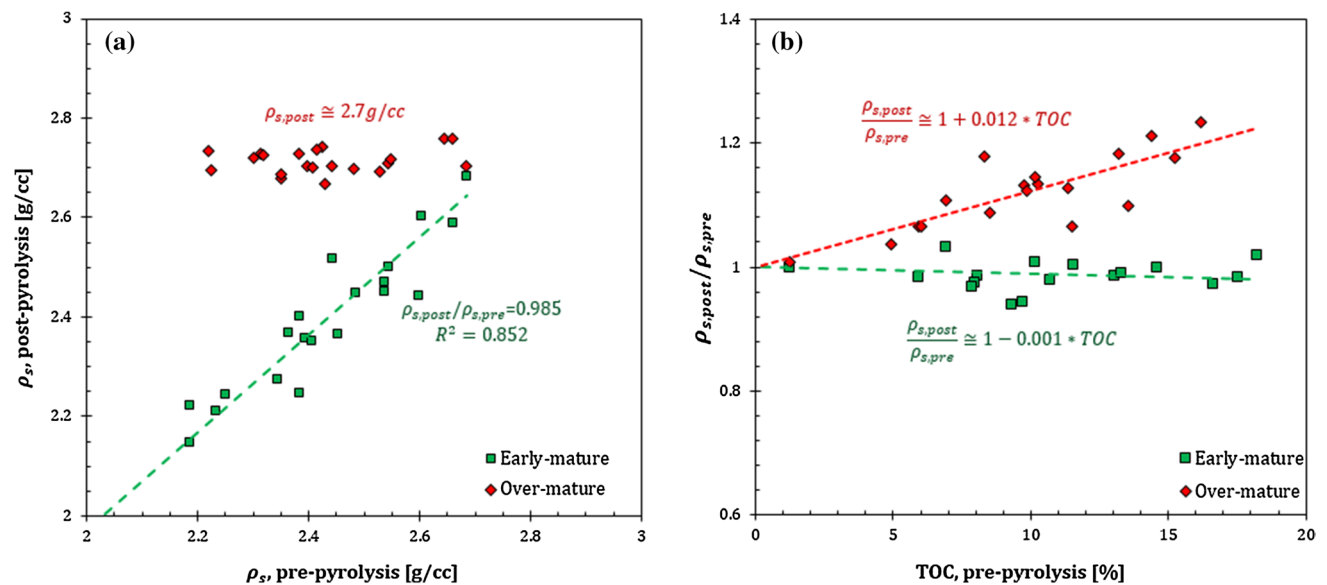

Fig. 4 Changes in solids density (ρ_s) upon unconfined pyrolysis (**a**) and their dependence on initial organic content (**b**)
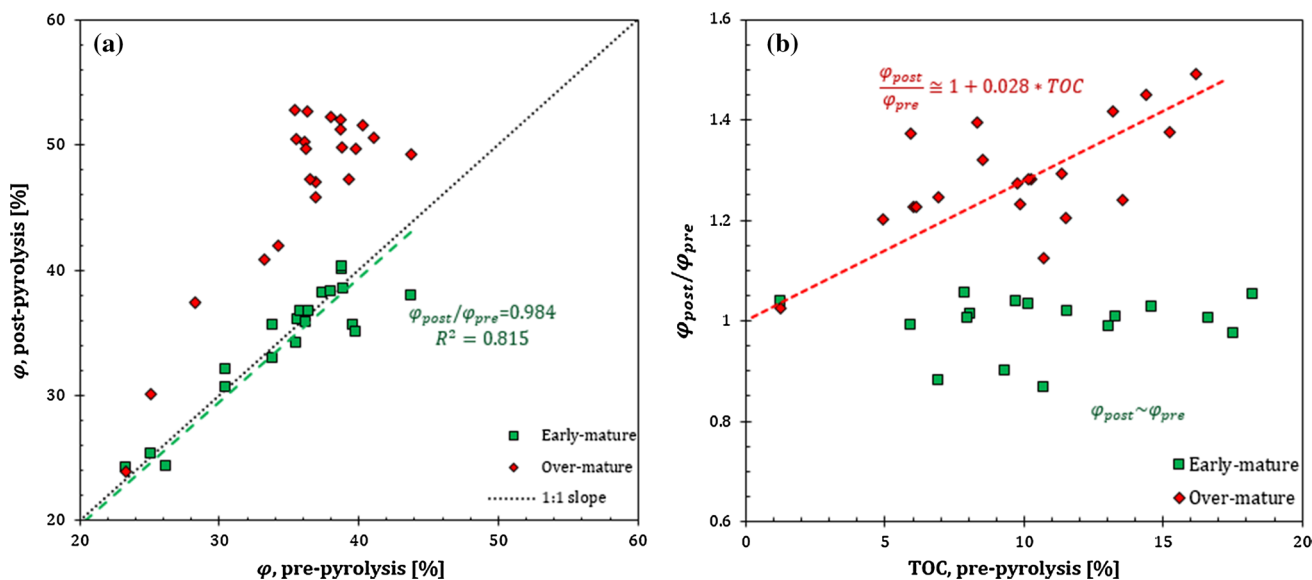
Fig. 5 Changes in porosity (φ) upon unconfined pyrolysis (**a**) and their dependence on initial organic content (**b**). The presented porosities are the measured values (not corrected for bitumen content)
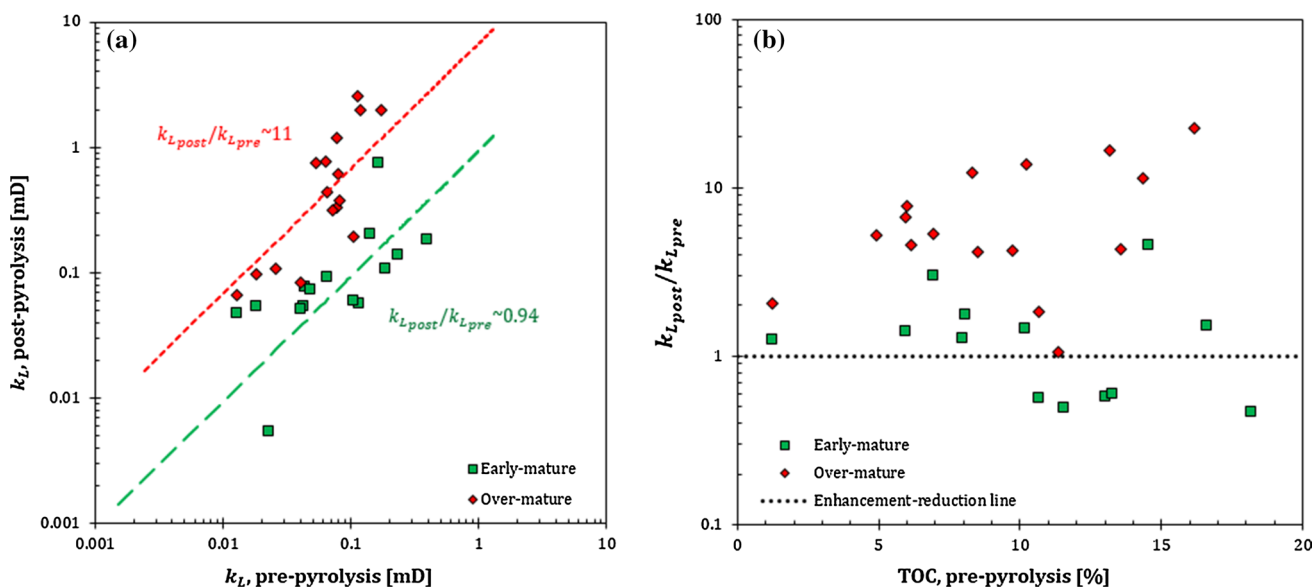

Fig. 6 Changes in the apparent liquid permeability (K_L) upon unconfined pyrolysis (**a**) and their dependence on initial organic content (**b**). Note that at the early-mature stage the permeability tends to decrease where TOC > 10% [plot below the dotted line in (**b**)]

to be nearly constant at a value of 2.7 g/cc (Fig. 4a). The shrinkage of the organic phase increases the porosity by a factor of ~ 1.29 (Fig. 5a). This shows that the initial organic content controls the rate of increase in solids density and porosity (Figs. 4b, 5b). The porosity increase causes a permeability enhancement by an order of magnitude (Fig. 6). Note that the post-pyrolysis results are consequent to unconfined pyrolysis, and the implication of the lack of backpressure will be elaborated in the discussion.

3.2 Acoustic Velocities and Rock Physics Modeling

In this paper, we present the bedding-normal acoustic velocities V_{p0} and V_{s0} (referred here as V_p and V_s) following pyrolysis and their relationships with immature rock velocities. The changes in V_p and V_s upon pyrolysis are presented in Fig. 7, where velocities were measured at the same stress levels as in the immature state. The observed petrophysical changes (Figs. 4, 5) result in the V_p decrease with increasing

maturation, because *P* waves are known to be sensitive to porosity and the pore-filling fluids. The *S* waves are less sensitive to changes in porosity but more to variations in the solid matrix, as they cannot travel through fluids. Consequently, the V_s displays an increase with increasing maturation (Fig. 7), despite the significant porosity enhancement. This is due to the densification and stiffening of the solid phase (see discussion section for further analysis). These trends of the acoustic velocities are directly connected to the elastic moduli in the bedding-normal direction: vertical oedometer modulus (C_{33}) and vertical shear modulus (C_{55}). These elastic moduli are used here to examine and calibrate effective elastic medium theories for the purpose of modeling and geoprospecting this high-porosity source rock.

Each maturity stage is modeled using Hashin–Shtrikman upper and lower bounds, and the measured C_{33} and C_{55} are used to create the best-fit "HS + BAM" curves. The "HS kerogen" curves are calculated as well, independently of the measurements. It is hard to determine the elastic properties of kerogen at different maturity levels because reported values have a wide range (e.g., Carcione 2001; Emmanuel et al. 2016; Vernik and Landis 1996; Yan and Han 2013; Zhao et al. 2016). Furthermore, most of the reported moduli neglect the influence of bitumen as if it does not exist, while here we address this issue using the diagram in Fig. 1. Summary of the values chosen for modeling each maturity stage is given in Table 2. We choose the Young's modulus of immature kerogen measured by Emmanuel et al. (2016) using atomic force microscopy (AFM), and by assuming kerogen Poisson's ratio of 0.3 the bulk and shear moduli of kerogen are obtained:

Fig. 7 Ratio between post-pyrolysis and pre-pyrolysis acoustic velocities (V_p and V_s), where the subscripts represent velocities at immature (IM), early-mature (EM) and over-mature (OM) states

$$K = \frac{E}{3(1 - 2\nu)} \tag{16}$$

$$\mu = \frac{E}{2(1 + \nu)} \tag{17}$$

Over-mature kerogen moduli are calculated using the same methodology, by combining data of over-mature rocks reported in Eliyahu et al. (2015) with a Poisson's ratio of 0.3. Early-mature kerogen moduli are believed to be a bit higher than the immature kerogen moduli due to slight kerogen stiffening and densification. Reported bitumen velocities (Han et al. 2006) are converted to elastic properties assuming density of ~ 1.05 g/cc. These velocities match approximately the bitumen modulus found in Zargari et al. (2013). The elastic moduli of the organic material (OM) are calculated here using Voigt type of averaging:

$$K_{om} = B_c K_{bit} + (1 - B_c) K_k \tag{18}$$

$$\mu_{om} = B_c \mu_{bit} + (1 - B_c) \mu_k \tag{19}$$

Equations (18) and (19) are then introduced to Eqs. (3)–(6) to create the models for the organic-rich chalk.

Graphical representation of the results is complex, as we have three independent dominant variables: porosity, organic content and maturation. For example (Fig. 8), the theoretical bounds may exhibit a smooth and continuous shape where organic content and maturity are set at a constant value and the only variable is porosity. However, we want to allow for variability of at least two of the independent parameters; thus, we use kerogen-factored porosity (first defined as "porosity-modified kerogen content" in Prasad et al. 2011; Shitrit et al. 2017). Kerogen-factored porosity is a sum of porosity and a fraction of the organic, leading to the smoothest shape of the best-fit "HS + BAM" curve of each modulus.

Measured and modeled results of oedometer modulus (Fig. 9) and shear modulus (Fig. 10) are plotted versus the kerogen-factored porosity. In each maturity stage, the measured values of C_{33} and C_{55} are used to create a best-fit "HS + BAM" model with a representative normalized stiffness factor ("w"). A fraction of 0.65 of the organic matter seems to optimize the smoothness of the best-fit curves at all maturity levels. Each plot includes a curve that simulates a kerogen-supported matrix ("HS kerogen"). A comparison between the measured and "HS kerogen" predicted moduli is given in Fig. 11. It can be seen that at the immature and early-mature states, the "HS kerogen" model predicts the vertical oedometer and shear moduli fairly well, while in the over-mature state, it overpredicts the measured data. This simply means that the post-pyrolysis samples at the over-mature state are extremely compliant due to extensive loss of solid
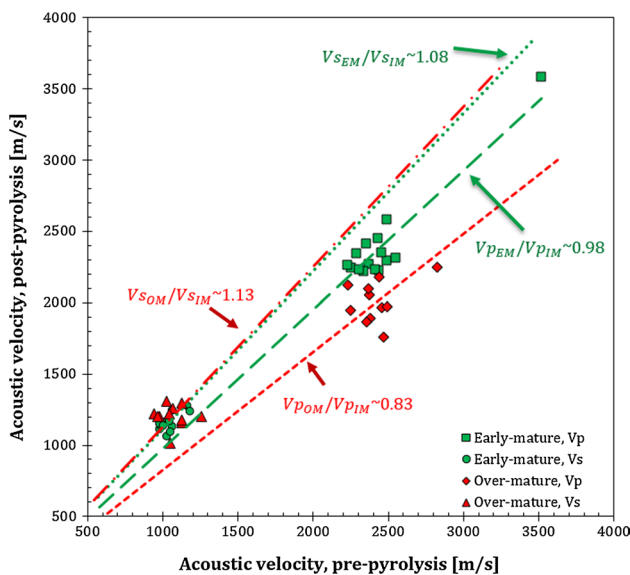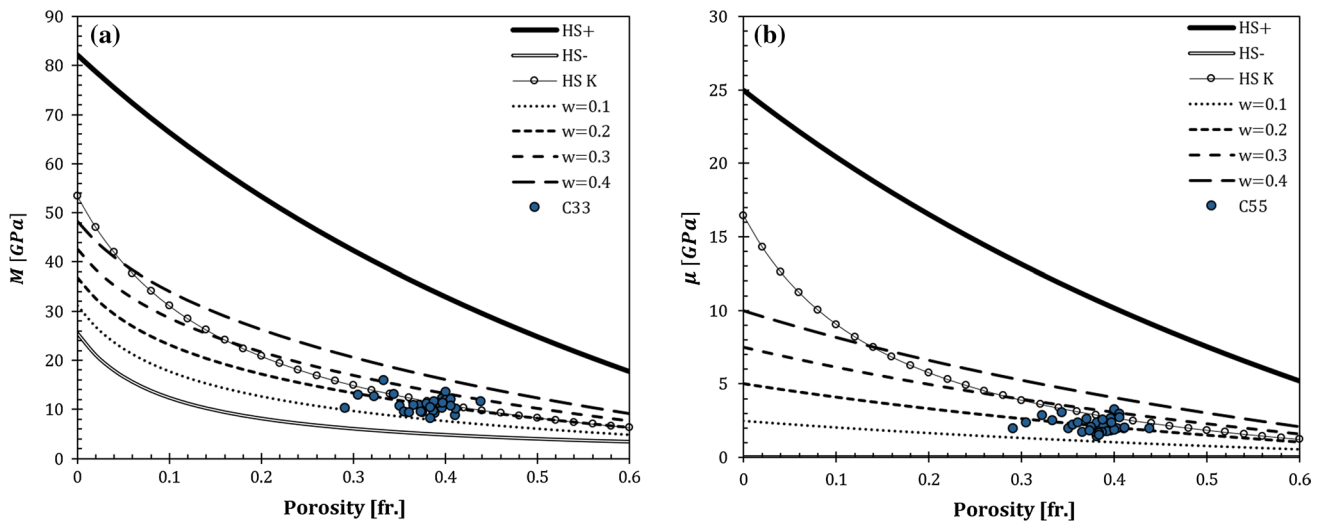
Fig. 8 Hashin–Shtrikman-based models of the dynamic oedometer modulus [M in (**a**)] and shear modulus [μ in (**b**)] at the immature state: The curves are continuous because a constant organic matter fraction (f_o) is set at 0.15, and the presented C_{33} and C_{55} results are within f_o range of 0.1–0.2. The presented models are the Hashin– Shtrikman upper (+), lower bound (−) and the intermediate "HS kerogen" curve (K). "HS + BAM" curves of different "w" values (normalized stiffness factors) are plotted to represent the typical span of stiffness of the immature organic-rich chalk. Note that in (**b**) the lower bound coincides with the horizontal axis
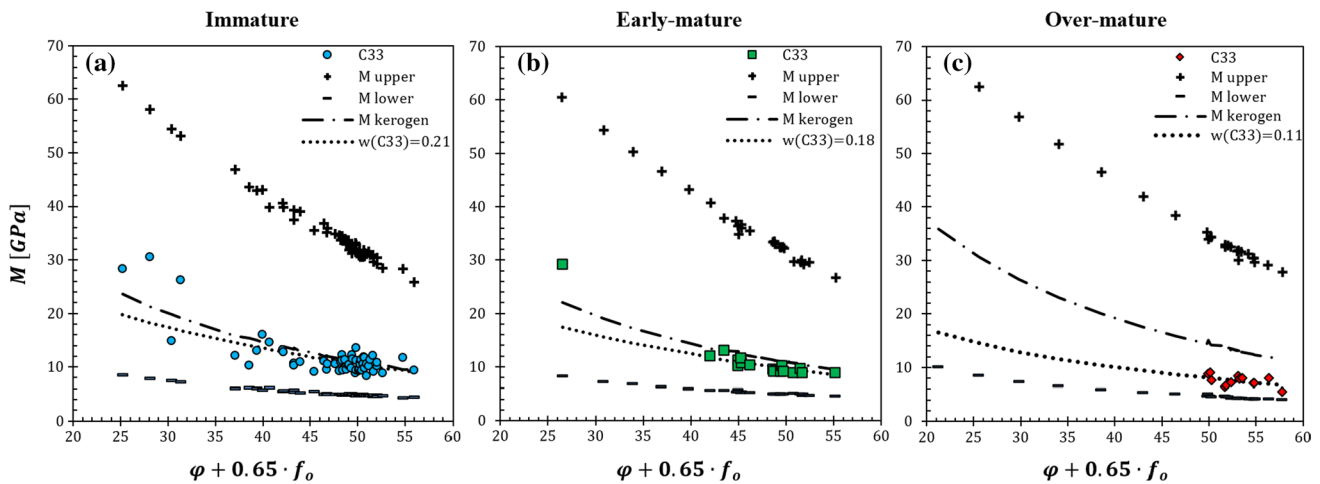
Fig. 9 Oedometer modulus ("M") dependency on soft phases at the three maturity stages: Three HS models represent a matrix that is mineral-supported ("M upper"), kerogen-supported ("M kerogen"), and fluid-suspended ("M lower"). The BAM curves are fitted to the measurements of vertical oedometer modulus (C_{33}) using the average normalized stiffness factor ("w_{C33}") observed at each maturity stage. The BAM-modeled curves at the three maturities are smoothed using a 0.65 fraction of the organic matter added to the porosity

volume and porosity enhancement at the absence of confining pressure. Over-mature rock porosity is believed to be significantly lower in naturally matured rocks primarily due to compaction, which would increase the normalized stiffness factors. To overcome the bias induced by unconfined pyrolysis, we postulate that a kerogen-supported rock model may be used to model the organic-rich chalk at different natural maturity levels. The contribution of this assumption is that porosity is allowed to change due to compaction, but the rock fabric remains kerogen-supported. The "HS + BAM" and "HS kerogen" models are further examined in the discussion.

4 Discussion

4.1 SEM Images

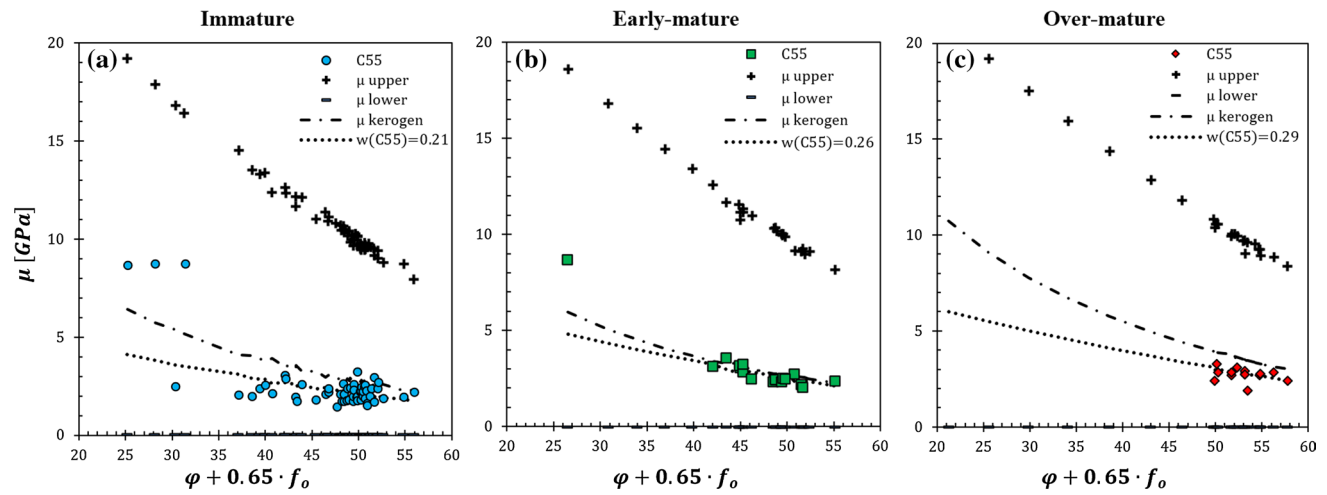Scanning electron microscopy (SEM) backscatter mode images at the three maturity stages are given in Fig. 12.

Fig. 10 Shear modulus ("μ") dependency on soft phases at the three maturity stages: Three HS models represent a matrix that is minerals-supported ("μ upper"), kerogen-supported ("μ kerogen") and fluid-suspended ("μ lower"). The BAM curves are fitted to the measurements of vertical shear modulus (C_{55}) using the average normalized stiffness factor ("w_{C55}") observed at each maturity stage. The BAM-modeled curves at the three maturities are smoothed using a 0.65 fraction of the organic matter added to the porosity
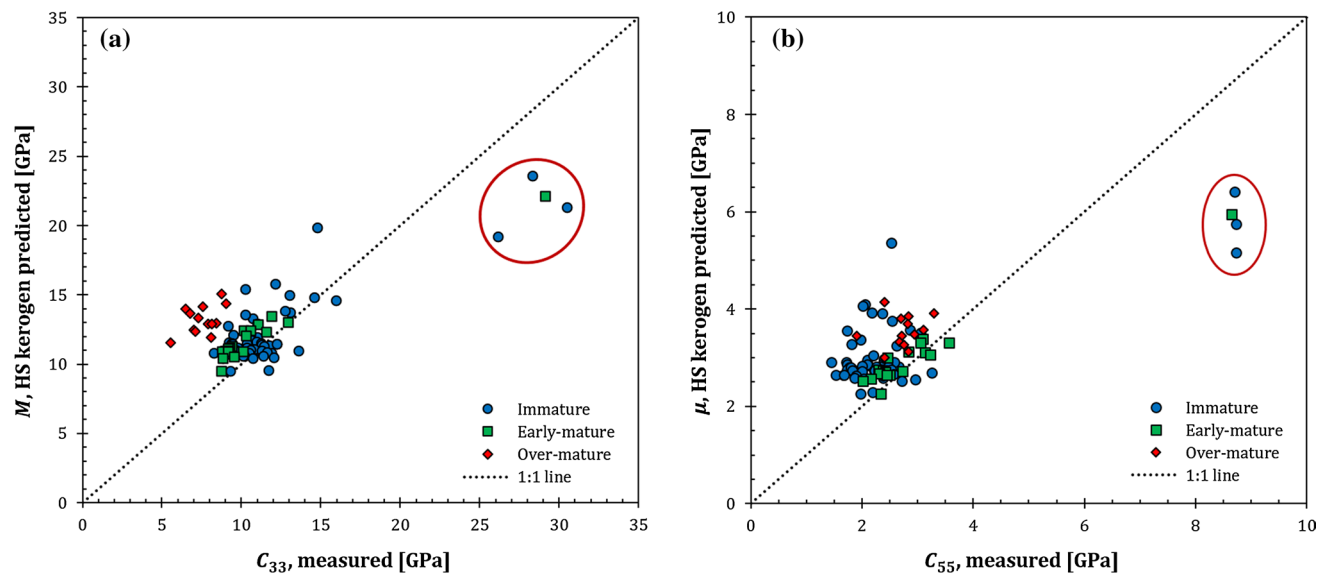

Fig. 11 Source rock stiffness template: "HS kerogen" predicted elastic moduli are cross-plotted against the measured vertical oedometer (**a**) and shear (**b**) moduli. Stiffened samples plot to the right of the 1:1 line (marked in the circles) and the more compliant samples plot to the left of it, like most of the over-mature measured data

Qualitative elemental analysis is enabled by energy-dispersive spectroscopy (EDS). The immature rock (Fig. 12a, b) displays a soft pore geometry pattern, where the fine-grained matrix is made of kerogen and micro-crystalline calcite, while coarser mineral grains "float" in this matrix. This explains why the "HS kerogen" model is predictive of the elastic moduli of the rock at the immature state (Figs. 9, 10, 11). The porosity includes three main types: stiff intra-calcite porosity, soft micro-nano-porosity inside the kerogen and inter-granular porosity. More detailed descriptions of the immature rock microstructure, including anisotropy and poroelastic parameters, are given in Shitrit et al. (2016, 2017). Kerogenous areas are identified at the micron scale, with a preferential bedding-parallel alignment. These areas appear in dark shades due to density contrast between the immature kerogen and the calcite. The normalized stiffness factors of vertical oedometer (w_{C33}) and shear (w_{C55}) moduli reflect the stiffness of the solid skeleton. Due to increased burial depth (~ 214 m), the sample in Fig. 12b is
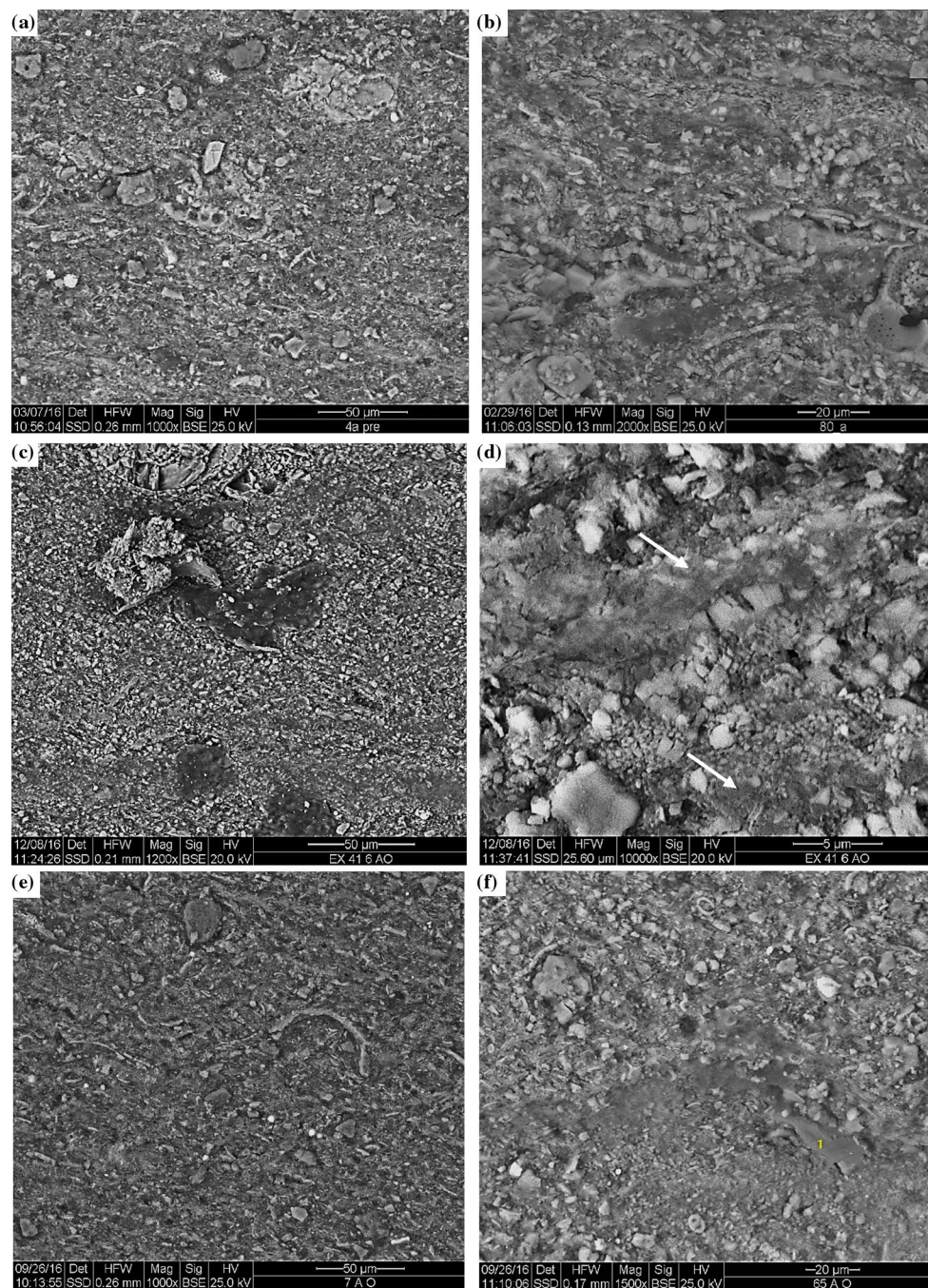
Fig. 12 SEM backscatter collection of the organic-rich chalk in its immature state (**a**, **b**), early-mature state (**c**, **d**) and over-mature state (**e**, **f**). Properties of the scanned samples: **a** immature rock, $\varphi = 39\%, f_o \cong f_k = 15\%, w_{C33} = 0.15, w_{C55} = 0.2$; **b** immature rock, $\varphi = 26\%, f_o \cong f_k = 25\%, w_{C33} = 0.26, w_{C55} = 0.18$; **c** and **d** early-mature rock, $\varphi = 36\%, f_{bit} = 4\%, f_k = 10\%, w_{C33} = 0.15, w_{C55} = 0.28$, white arrows point to bitumen flow texture (**d**); **e** over-mature rock, $\varphi = 47\%, f_{bit} = 1.5\%, f_k = 3\%, w_{C33} = 0.08, w_{C55} = 0.28$; **f** over-mature rock, $\varphi = 47\%, f_{bit} = 1.2\%, f_k = 2.5\%, w_{C33} = 0.1, w_{C55} = 0.27$, pure organic matter is detected (marked by "1"). The observations from this figure are given in Sect. 4.1 in the discussion

more compacted and cemented than the sample in Fig. 12a, and consequently, w_{C33} is higher.

In the early-mature state, the rock preserves the density contrast between the kerogen and the minerals. At this stage, the bitumen content is relatively high. The high bitumen content is uniquely attributed to sulfur-rich source rocks (Baskin and Peters 1992), where carbon–sulfur bonds are cracked early in the maturation process to produce bitumen. Bituminous zones can be identified by extremely dark areas (Fig. 12c) that seem to spread radially in the matrix from
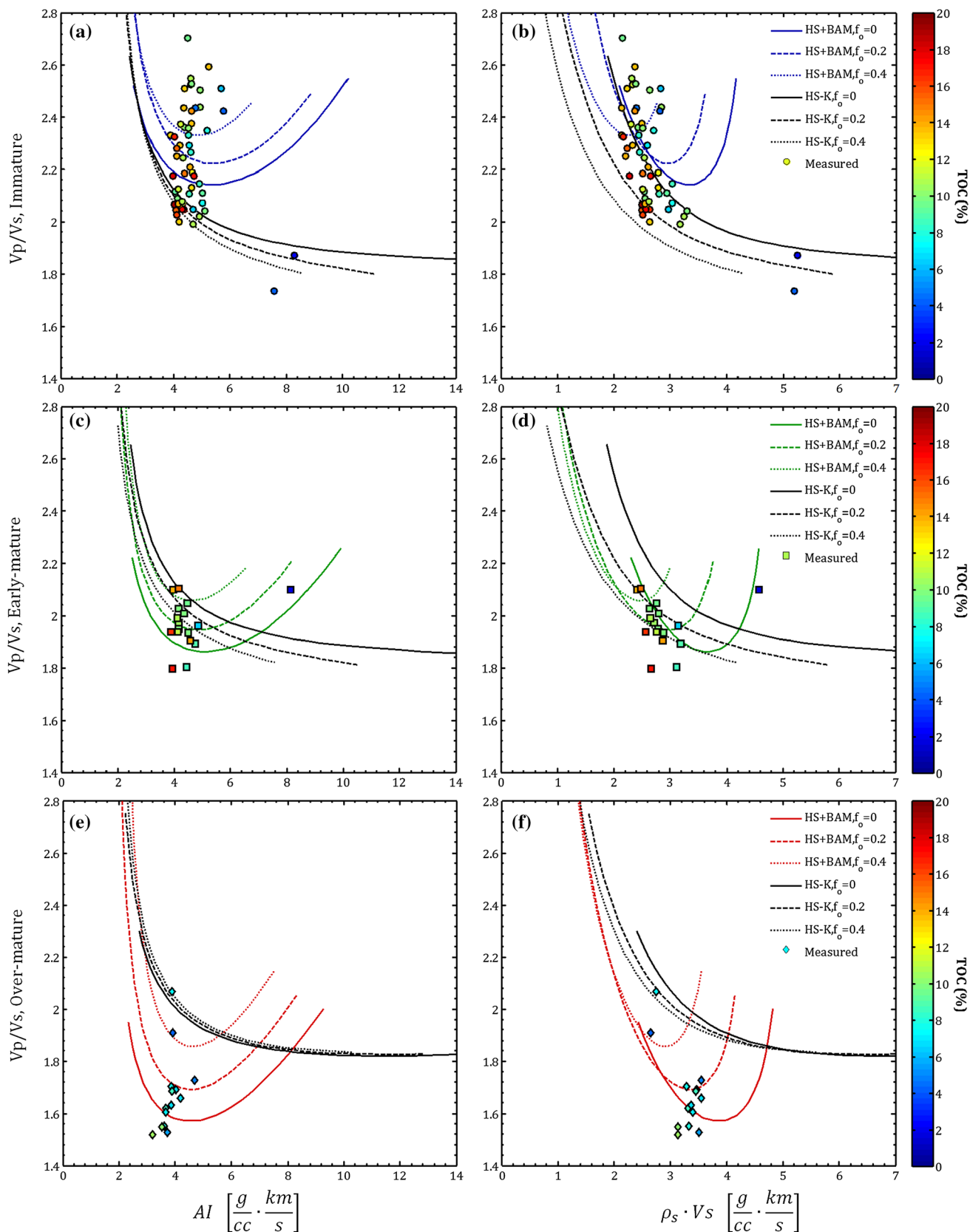
Rock physics templates of the organic-rich chalk at immature (**a**, **b**), early-mature (**c**, **d**) and over-mature (**e**, **f**) states. Traditional presentation of V_p/V_s versus the acoustic impedance (AI) of the rock is on the left panel (**a**, **c**, **e**), and versus the product of solids density and V_s ($\rho_s \cdot V_s$) on the right panel (**b**, **d**, **f**). Three curves of each model at a certain maturity stage are drawn to simulate organic matter volume fractions (f_o) of 0 (dotted line), 0.2 (dashed line) and 0.4 (solid line). The "HS + BAM" curves are better fitted to the experimental post-pyrolysis data, and the "HS-K" curves represent a kerogen-supported rock model which seems more representative of naturally matured organic-rich chalk. The color-coded measured points reflect an organic enrichment trend toward low V_p/V_s and AI or $\rho_s \cdot V_s$ (bottom left area of the figures)

kerogen-rich areas. They may also be identified by flow texture (Fig. 12d) that records the bitumen invasion into preexisting pores during the maturation. These two observations propose a source for w_{C33} decrease from 0.25 to 0.15 following pyrolysis-induced early maturation measured on splits of the same core sample. The w_{C55} on the other hand shows a slight increase from 0.25 to 0.28, possibly because of kerogen stiffening, but this inference requires more data.

The most prominent changes occur at the over-mature stage. The density contrast becomes much less distinctive (Fig. 12e, f) due to kerogen densification. The organic material has the same proportions as in the early-mature state with approximately 30% bitumen and 70% kerogen, only that the kerogen here exhausted the entire potential of hydrocarbon expulsion. This results in a drastic volume decrease in the organic phase. Severe porosity enhancement is taking place within the kerogen, so that the scanned rock samples are nearly 50% made of voids, although it is not easily seen in the images (Fig. 12e, f). This is attributed to newly generated nanoscale kerogen porosity. The residual amounts of bitumen and the enhanced porosity in the kerogen cause the organic-rich zones to appear somewhat darker than the minerals. A pure organic matter in Fig. 12f, detected by EDS spotting, exhibits bright shades almost as much as the surrounding calcite grains. The notions listed here are important for examining the unusually high kerogen densities encountered at the over-mature state. The post-pyrolysis rock matrix is very compliant at this stage, indicated by $w_{C33} \leq 0.1$, due to high porosity of the pyrolyzed core samples. The opposite trend of shear stiffening, evident by $w_{C55} \sim 0.28$, is caused by significant increase in kerogen density and stiffness.

4.2 Rock Physics Templates

Rock physics templates typically refer to a plot of V_p/V_s ratio versus acoustic impedance "AI" ($= \rho_b V_p$). For this purpose, we model the behavior of the organic-rich chalk at the immature (Fig. 13a), early-mature (Fig. 13c) and over-mature states (Fig. 13e). In each modeled curve, we need to set constant two of the three dominant variables: porosity, organic content and maturation. The templates are presented for each

maturity stage separately, and in each plot, there are three curves for different organic contents (f_o). This way, porosity is the free variable in the modeled curves. As mentioned earlier, we calculate two types of Hashin–Shtrikman-oriented models: the experimentally fitted "HS + BAM" model and the "HS kerogen" model. Using the "HS kerogen" model, we assume that the rock remains kerogen-supported during maturation regardless of the porosity, thus less prone to deviations due to different stress states. Since the core samples were not subjected to compaction during the pyrolysis, high core porosities were measured. As a result, the acoustic impedance measured here is probably lower than in naturally matured rocks. We propose a plot of V_p/V_s ratio versus the product of solids density and shear velocity ($\rho_s \cdot V_s$) to diminish porosity-induced deviations (Fig. 13b, d, f). Model calculations are based on the predicted oedometer and shear moduli, as presented above. In order to compute acoustic velocities, AI and $\rho_s \cdot V_s$, the bulk density and solids density are calculated by:

$$\rho_b = \varphi \rho_w + f_o \rho_o + (1 - \varphi - f_o)\rho_m \qquad (20)$$

$$\rho_s = \frac{f_o}{1 - \varphi}\rho_o + \frac{1 - \varphi - f_o}{1 - \varphi}\rho_m \qquad (21)$$

To observe the effect of maturation, the curves of 0.2 volume fraction of the organic matter at the three maturity stages are presented in a single template in Fig. 14.

It is seen that the "HS + BAM" curves span over a large V_p/V_s range due to the state of the pyrolyzed samples. These curves exhibit a "U" shape because they predict a steep increase in M toward zero porosity, which is not compensated by a steep increase in μ in the same zone (Fig. 8). On the contrary, the "HS kerogen" model predicts a steep increase in both M and μ at the vicinity of zero porosity; hence, the "L" shape of the curves is observed. This shape seems much more realistic as rock physics studies of source rocks do not report V_p/V_s increase at high acoustic impedance values (e.g., Avseth and Carcione 2015; Lucier et al. 2011; Zhao et al. 2016). The "HS kerogen" curves appear very close to each other at the three maturity stages (Fig. 14), because the changes in elastic moduli of the organic components due to maturation are small compared to the effect of porosity and organic content. Therefore, the "HS kerogen" curves are less indicative of thermal maturation, and more diagnostic of porosity and organic content. Both models show a decrease in V_p/V_s with increasing maturation in a typical rock physics template (Fig. 14a). This general trend has been seen before in organic-rich shale modeling (Bredesen et al. 2015; Zhao et al. 2016), but the curves are shifted to higher values of acoustic impedance, as well as the point of maximum curvature. This is because organic-rich shales are naturally much less porous than the organic-rich chalk. The measured values (color-coded data points in Fig. 13) indicate
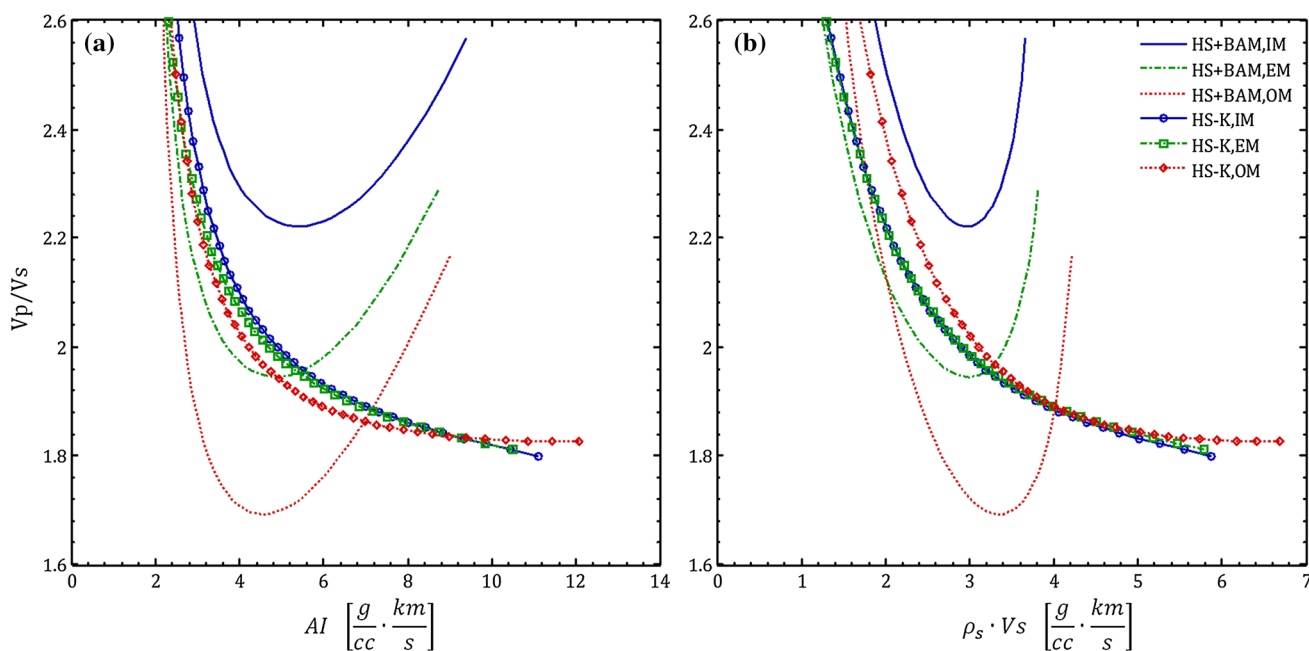
Fig. 14 Templates of immature (IM), early-mature (EM) and over-mature (OM) states are made using the experimentally fitted "HS + BAM" curves and the conceptual "HS kerogen" curves (HS-K). Organic matter volume fraction is set equal to 0.2

an organic enrichment trajectory toward low V_p/V_s ratio and acoustic impedance, which is also found typical to organic-rich shales (Lucier et al. 2011; Zhao et al. 2016). The organic enrichment trajectory of the "HS kerogen" curves appears consistent with this trend, but the opposite direction is seen in the "HS + BAM" curves (Fig. 13). The pattern of the "HS + BAM" curves is therefore less representative of a naturally matured rock for two main reasons. First, Marion's BAM model is designed for fluid substitution in a rock at a certain state, and different porosities may lead to different values of "w". Second, the unconfined conditions in the pyrolysis resulted in extremely loose grain packing which is not believed to occur in natural conditions. Therefore, we believe that the "HS kerogen" model is more applicable than the "HS + BAM" for geophysical exploration. Preliminary examination of Niobrara chalk reported velocities at water-saturated conditions with lower porosity (Vernik and Liu 1997) confirms the "HS kerogen" model is predictive. Further investigation of these trends will be performed using results from another basin in which the Ghareb and Mishash formations are buried deeper (preliminary results are given in Gordin et al. 2016). Plotting the V_p/V_s ratio against the $\rho_s \cdot V_s$ (Figs. 13b, d, f, 14b) seems to pronounce the differences in organic content and maturation better than using a typical rock physics template (Figs. 13a, c, e, 14a). For this reason, we believe that comparison between source rocks from different basins is better done using a template of V_p/V_s ratio versus $\rho_s \cdot V_s$, in order to highlight the changes within

the solid matrix and the organic matter and lessen the effect of porosity and pore pressure.

4.3 Applicability of the Post-pyrolysis Results

Looking at the whole analysis of pyrolyzed rock samples made in this paper, there are few issues that require further examination. First, it is questionable how much do the pyrolysis experiments simulate the thermal maturation process. The pyrolysis experiments were performed at unconfined, anhydrous (water-free) conditions. Porosity enhancement should ideally be followed by compaction, although the post-pyrolysis porosity evolved under unconfined conditions. Hence, naturally matured samples are expected to be less porous. An attempt for simulating field conditions in the acoustic measurements was made, but strain in organic-rich rocks may be time-dependent (Yang and Zoback 2016) and pressures applied in the laboratory did not introduce sufficient strain into the samples. Previous pyrolysis experiments of the studied organic-rich chalk formations (Bisnovat 2013) examined the effect of 150 psi (1 MPa) backpressure on the pyrolysis process. Compared to unconfined pyrolysis, the petrophysical results were found similar, only that TOC loss in the pressurized experiment was slightly lower. Discrepancies may also originate from other sources such as exaggerated microcracking in unconfined pyrolysis (Allan et al. 2014). We do believe that conducting the pyrolysis experiment under confined conditions (e.g., Gayer 2015) would yield a better replication of natural maturation. Geochemical

alterations at the absence of water (as in anhydrous pyrolysis) may cause additional deviations from natural maturation conditions. Hydrous pyrolysis experiments on Irati oil shale (Gayer 2015) indicate higher conversion rates of kerogen to hydrocarbons than in anhydrous pyrolysis. However, in carbonates this difference is minor (Koopmans et al. 1998). The deviations mentioned here should be accounted for when extrapolating rock properties from artificially to naturally matured states. In this paper, we attempt to do that by using the kerogen-supported matrix model, which may require further refinements relating to microcracking and the state of the organic material.

The permeability measurements indicate decrease in mean pore radius in the post-pyrolysis samples. This may be attributed to bitumen choking of pre-existing pores or development of nano-porosity in kerogen during maturation (Bernard et al. 2012; Loucks et al. 2012). Permeability has been reported to reach minimum values at mature level (%Ro = 0.88) where bitumen saturation is high (Ghanizadeh et al. 2014). However, applicability of gas permeability measurements to tight organic-rich rocks should be considered. Klinkenberg's gas slippage effect is important in tight rocks (Tanikawa and Shimamoto 2009), but the pressure dependence is nonlinear (Moghadam and Chalaturnyk 2014). Klinkenberg-corrected permeability may exhibit large scatter due to kinetic effects of the gas molecules in nano-capillaries (Fathi et al. 2012). Further deviations may be caused where matrix stiffness is considerably low and poroelasticity-based pressure corrections are required (Wang et al. 2014). Our permeability analysis is simplified to obtain some sense regarding permeability evolution during maturation, and the mentioned sources for errors are beyond the scope of this study. Further research in this direction shall include adjustments of laboratory experimentation and theoretical approaches to better analyze the organic-rich chalk.

Our results indicate high organic material density (~ 2.4 g/cc) at the over-mature state, which leads to strikingly high kerogen density (~ 3 g/cc). Values of over-mature kerogen density reported in the literature were never found to exceed 1.6 g/cc (Alfred and Vernik 2012; Okiongbo, Aplin and Larter 2005; Vernik and Nur 1992). On the other hand, most rock physics models take into account extrapolated kerogen properties, which are lower than direct stiffness measurements using AFM or nano-indentation (Eliyahu et al. 2015; Emmanuel et al. 2016; Zargari et al. 2016). It is also possible that bitumen saturation inside over-mature kerogens has been overlooked. The high kerogen density results here from the physical relationship between solids density and TOC. The increase in shear wave velocity and the lowering of the contrast in backscatter SEM images at the over-mature state also align with this observation. Solids density increase may be attributed to pyrite precipitation and graphite generation, but only to a restricted extent. It is also possible that the sulfur that remains in the organic material contributes to the density increase in an over-mature type IIS kerogen. Yet, the over-mature high density values reported here are planned for further examination by different testing methods such as nano-indentation, AFM and X-ray diffraction analyses.

5 Summary and Conclusions

The effect of unconfined pyrolysis-induced maturation on rock physics of organic-rich chalk is examined here using petrophysical and acoustic measurements. Post-pyrolysis rock properties at early-mature and over-mature states are compared with the native (immature) rock properties. We analyze the data using careful differentiation between bitumen and kerogen and selection of their elastic moduli, in order to model properly the elastic properties of the organic-rich chalk at different maturity levels. Hashin–Shtrikman-based models are used to analyze the measured data and extrapolate to natural conditions. The post-pyrolysis data collected here lead to the following conclusions:

1. During maturation, the true porosity is enhanced by a factor of 1.09 at the early-mature state and by 1.29 at the over-mature state. Porosity measurements at the early-mature state show lower porosity than at the immature state due to bitumen generation and invasion to pre-existing pores. The porosity enhancement at the over-mature stage causes a permeability increase by an order of magnitude.

2. Using the data of porosity, solids density, TOC and bitumen extraction experiments, we observe moderate increase in kerogen density from 1.43 g/cc at the immature stage, to ~ 1.47 at the early-mature stage, and considerably greater up to 2.98 g/cc at the over-mature stage. The density of the entire organic phase, including bitumen content, somewhat decreases from 1.43 to 1.34 g/cc at the early-mature state and increases to 2.4 g/cc at the over-mature state. High kerogen densities are also implied from backscatter SEM images and increased S wave velocity. The resulting kerogen densities are much higher than values reported in the literature, possibly due to high sulfur content or precipitation of dense minerals during the pyrolysis. Nevertheless, these mechanisms are not sufficient to explain the magnitude of the discrepancy and further nanoscale measurements are required to confirm the reported densities.

3. The acoustic velocities show diverging trends for V_p and V_s upon pyrolysis: V_p decreases due to porosity enhancement, while V_s increases due to densification and stiffening of the post-pyrolysis solid matrix. Rep-

resentative BAM normalized stiffness factors depict a similar behavior: at the immature, early-mature and over-mature stages, w_{C33} decreases from 0.21 to 0.18 and 0.11, respectively, and w_{C55} increases from 0.21 to 0.26 and 0.29, respectively.

4. The mean pore radius decreases from ~ 500 nm at the immature stage to ~ 200 nm after pyrolysis due to significant increase in nanoscale kerogen porosity and bitumen generation.

While pyrolysis is aimed to simulate thermal maturation, a true replication of natural maturation is restricted by the absence of ambient field conditions such as compaction, slow heating rate, fluid saturations, pore pressure and time-dependent response of the mineralogical matrix. Specifically, the lack of compaction seems the most crucial in our case, and in order to overcome this, a Hashin–Shtrikman kerogen-supported matrix model ("HS kerogen") is used to estimate the elastic moduli. Rock physics templates, made by using both "HS + BAM" and "HS kerogen" models, suggest that a kerogen-supported rock model provides more realistic estimations by showing better similarity to trends typical to naturally matured organic-rich rocks. Nevertheless, tracing maturation trends in a typical rock physics template is less applicable in such a high-porosity rock as the organic-rich chalk, due to the inherent mechanical dominance of the porosity. In order to make the representation more focused on changes in the solid matrix, we also use a V_p/V_s versus $\rho_s \cdot V_s$ plot. This type of plot can be used to compare between different basins or different types of source rock with similar mineralogy using the same template.

References

Alfred D, Vernik L (2012) A new petrophysical model for organic shales. Paper presented at the SPWLA 53rd annual logging symposium

Allan AM, Vanorio T, Dahl JE (2014) Pyrolysis-induced P-wave velocity anisotropy in organic-rich shales. Geophysics 79(2):D41–D53

American Petroleum Institute (API) (1998) Recommended practices for core analysis. (No. 40, 2nd edn. American Petroleum Institute, Exploration and Production Department, Washington, DC

Avseth P, Carcione JM (2015) Rock-physics analysis of clay-rich source rocks on the Norwegian Shelf. Lead Edge 34(11):1340–1348

Avseth P, Mukerji T, Mavko G, Dvorkin J (2010) Rock-physics diagnostics of depositional texture, diagenetic alterations, and reservoir heterogeneity in high-porosity siliciclastic sediments and rocks—A review of selected models and suggested work flows. Geophysics 75(5):75A31–75A47

Baskin DK, Peters KE (1992) Early generation characteristics of a sulfur-rich Monterey Kerogen. AAPG Bull 76(1):1–13

Bernard S, Horsfield B, Schulz H, Wirth R, Schreiber A, Sherwood N (2012) Geochemical evolution of organic-rich shales with increasing maturity: a STXM and TEM study of the Posidonia Shale (Lower Toarcian, Northern Germany). Mar Pet Geol 31(1):70–89

Bisnovat K (2013) Mechanical and petrophysical behavior of oil shale from the Judea Plains, Israel. M.Sc. thesis, Ben-Gurion University of the Negev, Israel

Bisnovat K, Hatzor YH, Vinegar HJ, Nguyen SV, Palchik V, Feinstein S (2015) Mechanical and petrophysical behavior of organic-rich chalk from the Judea Plains, Israel. Mar Pet Geol 64:152–164

Bredesen K, Jensen EH, Johansen TA, Avseth P (2015) Seismic reservoir and source-rock analysis using inverse rock-physics modeling: a Norwegian Sea demonstration. Lead Edge 34:1350–1355

Bridges M (2016) Mechanical properties of the Niobrara. M.Sc. thesis, Colorado School of Mines, Golden, Colorado. http://hdl.handle.net/11124/170636

Carcione JM (2001) AVO effects of a hydrocarbon source-rock layer. Geophysics 66(2):419–427

Carcione JM, Avseth P (2015) Rock-physics templates for clay-rich source rocks. Geophysics 80(5):D481–D500

Carcione JM, Helle HB, Avseth P (2011) Source-rock seismic-velocity models: Gassmann versus Backus. Geophysics 76(5):N37–N45

Eliyahu M, Emmanuel S, Day-Stirrat RJ, Macaulay CI (2015) Mechanical properties of organic matter in shales mapped at the nanometer scale. Mar Pet Geol 59:294–304

Emmanuel S, Eliyahu M, Day-Stirrat RJ, Hofmann R, Macaulay CI (2016) Impact of thermal maturation on nano-scale elastic properties of organic matter in shales. Mar Pet Geol 70:175–184

Fabricius IL (2003) How burial diagenesis of chalk sediments controls sonic velocity and porosity. AAPG Bull 87(11):1755–1778

Fabricius IL, Bächle GT, Eberli GP (2010) Elastic moduli of dry and water-saturated carbonates—effect of depositional texture, porosity, and permeability. Geophysics 75(3):N65–N78

Fathi E, Tinni A, Akkutlu IY (2012) Correction to Klinkenberg slip theory for gas flow in nano-capillaries. Int J Coal Geol 103:51–59

Gayer JL (2015) Artificial maturation of oil shale: the Irati formation from the Paraná Basin, Brazil. M.Sc. thesis, Colorado School of Mines, Golden, Colorado

Ghanizadeh A, Amann-Hildenbrand A, Gasparik M, Gensterblum Y, Krooss BM, Littke R (2014) Experimental study of fluid transport processes in the matrix system of the European organic-rich shales: II. Posidonia Shale (Lower Toarcian, Northern Germany). Int J Coal Geol 123:20–33

Golder Associates (2011) Zoharim in situ stress measurement—hydraulic jacking. (No. 113-81968). Golder Associates, Tel Aviv

Gordin Y, Hatzor YH, Vinegar HJ (2016) Ultrasonic velocity and anisotropy of organic-rich chalks. American Rock Mechanics Association (ARMA), Houston

Han D, Liu J, Batzle M (2006) Acoustic property of heavy oil-measured data. Paper presented at the SEG technical program expanded abstracts 2006, New Orleans, pp 1903–1907

Hofmann R (2006) Frequency dependent elastic and anelastic properties of clastic rocks. Ph.D. thesis, Colorado School of Mines, Golden, Colorado

Klinkenberg L (1941) The permeability of porous media to liquids and gases. Paper presented at the drilling and production practice, New York, NY, USA, pp 200–213

Koopmans M, Carson F, Damsté JS, Lewan M (1998) Biomarker generation from type II-S kerogens in claystone and limestone during hydrous and anhydrous pyrolysis. Org Geochem 29(5):1395–1402

Kutuzov I (2017) Study of the early stage immature oil produced from the israeli oil shale. Unpublished M.Sc. thesis. Ben-Gurion University of the Negev, Be'er Sheva, Israel

Labani MM, Rezaee R (2015) The importance of geochemical parameters and shale composition on rock mechanical properties of gas shale reservoirs: a case study from the Kockatea Shale and Carynginia Formation from the Perth Basin, Western Australia. Rock Mech Rock Eng 48(3):1249

Løseth H, Wensaas L, Gading M, Duffaut K, Springer M (2011) Can hydrocarbon source rocks be identified on seismic data? Geology 39(12):1167–1170

Loucks RG, Reed RM, Ruppel SC, Hammes U (2012) Spectrum of pore types and networks in mudrocks and a descriptive classification for matrix-related mudrock pores. AAPG Bull 96(6):1071–1098

Lucier AM, Hofmann R, Bryndzia LT (2011) Evaluation of variable gas saturation on acoustic log data from the Haynesville Shale gas play, NW Louisiana, USA. Lead Edge 30(3):300–311

Marion DP (1990) Acoustical, mechanical, and transport properties of sediments and granular materials. Ph.D. thesis, Stanford University, CA, US

Mavko G, Mukerji T, Dvorkin J (2009) The rock physics handbook: tools for seismic analysis of porous media. Cambridge University Press, Cambridge

Meilijson A, Ashckenazi-Polivoda S, Ron-Yankovich L, Illner P, Alsenz H, Speijer RP, Almogi-Labin A, Feinstein S, Berner Z, Püttmann W (2014) Chronostratigraphy of the upper cretaceous high productivity sequence of the southern Tethys, Israel. Cretac Res 50:187–213

Modica CJ, Lapierre SG (2012) Estimation of kerogen porosity in source rocks as a function of thermal transformation: example from the Mowry Shale in the Powder River Basin of Wyoming. AAPG Bull 96(1):87–108

Moghadam AA, Chalaturnyk R (2014) Expansion of the Klinkenberg's slippage equation to low permeability porous media. Int J Coal Geol 123:2–9

Okiongbo KS, Aplin AC, Larter SR (2005) Changes in type II kerogen density as a function of maturity: evidence from the Kimmeridge Clay Formation. Energy Fuels 19(6):2495–2499

Olsen C (2007) Elastic and electric properties of North Sea Chalk. Ph.D. thesis, Technical University of Denmark, Department of Civil Engineering, Arctic Technology Centre, ARTEK, Kongens Lyngby, Denmark

Orr WL (1986) Kerogen/asphaltene/sulfur relationships in sulfur-rich Monterey oils. Org Geochem 10(1–3):499–516

Prasad M, Mba KC, Sadler T, Batzle ML (2011) Maturity and impedance analysis of organic-rich shales. SPE Reserv Eval Eng 14(05):533–543

Qin X, Han D, Yan F (2016) Rock-physics modeling of shale during smectite-to-illite transition. Paper presented at the SEG international exposition and 86th annual meeting, 2016, Dallas, TX, US, pp 3416–3421

Ryan RC, Fowler TD, Beer GL, Nair V (2010) Shell's in situ conversion process—from laboratory to field pilots. In: Ogunsola OI, Hartstein AM, Ogunsola O (Eds) Oil shale: a solution to the liquid fuel dilemma, ACS Symposium Series 1032. American Chemical Society, Washington, DC, pp 161–183

Sayers CM (2013) The effect of anisotropy on the Young's moduli and Poisson's ratios of shales. Geophys Prospect 61(2):416–426

Shitrit O, Hatzor YH, Feinstein S, Palchik V, Vinegar HJ (2016) Effect of kerogen on rock physics of immature organic-rich chalks. Mar Pet Geol 73:392–404

Shitrit O, Hatzor YH, Feinstein S, Palchik V, Vinegar HJ (2017) Static and dynamic elastic moduli of organic-rich chalk. Geophys Prospect (**submitted**)

Sone H, Zoback MD (2013) Mechanical properties of shale-gas reservoir rocks—part 1: static and dynamic elastic properties and anisotropy. Geophysics 78(5):D381–D392

Suarez-Rivera R, Fjær E (2013) Evaluating the poroelastic effect on anisotropic, organic-rich, mudstone systems. Rock Mech Rock Eng 46(3):569–580

Sweeney JJ, Burnham AK (1990) Evaluation of a simple model of vitrinite reflectance based on chemical kinetics (1). AAPG Bull 74(10):1559–1570

Tanikawa W, Shimamoto T (2009) Comparison of Klinkenberg-corrected gas permeability and water permeability in sedimentary rocks. Int J Rock Mech Min Sci 46(2):229–238

Vanorio T, Mukerji T, Mavko G (2008) Emerging methodologies to characterize the rock physics properties of organic-rich shales. Lead Edge 27(6):780–787

Vernik L, Landis C (1996) Elastic anisotropy of source rocks: implications for hydrocarbon generation and primary migration. AAPG Bull 80(4):531–544

Vernik L, Liu X (1997) Velocity anisotropy in shales: a petrophysical study. Geophysics 62(2):521–532

Vernik L, Milovac J (2011) Rock physics of organic shales. Lead Edge 30(3):318–323

Vernik L, Nur A (1992) Ultrasonic velocity and anisotropy of hydrocarbon source rocks. Geophysics 57(5):727–735

Villamor Lora R, Ghazanfari E, Asanza Izquierdo E (2016) Geomechanical characterization of marcellus shale. Rock Mech Rock Eng 49:3403–3424

Wang Z, Wang H, Cates ME (2001) Effective elastic properties of solid clays. Geophysics 66(2):428–440

Wang G, Wang T, Simoneit BR, Zhang L, Zhang X (2010) Sulfur rich petroleum derived from lacustrine carbonate source rocks in Bohai Bay Basin, East China. Organ Geochem 41(4):340–354

Wang G, Ren T, Wang K, Zhou A (2014) Improved apparent permeability models of gas flow in coal with Klinkenberg effect. Fuel 128:53–61

Yan F, Han D (2013) Measurement of elastic properties of kerogen. Paper presented at the 2013 SEG annual meeting, Houston, Texas. doi:10.1190/segam2013-1319.1

Yang Y, Zoback M (2016) Viscoplastic deformation of the Bakken and adjacent formations and its relation to hydraulic fracture growth. Rock Mech Rock Eng 49(2):689

Zargari S, Prasad M, Mba KC, Mattson ED (2013) Organic maturity, elastic properties, and textural characteristics of self resourcing reservoirs. Geophysics 78(4):D223–D235

Zargari S, Wilkinson TM, Packard CE, Prasad M (2016) Effect of thermal maturity on elastic properties of kerogen. Geophysics 81(2):M1–M6

Zhao L, Qin X, Han D, Geng J, Yang Z, Cao H (2016) Rock-physics modeling for the elastic properties of organic shale at different maturity stages. Geophysics 81(5):D527–D541